Received: 15 July 2021 | Revised: 23 December 2021 | Accepted: 24 December 2021

DOI: 10.1002/mp.15464

RESEARCH ARTICLE

MEDICAL PHYSICS

Deformability of ascending thoracic aorta aneurysms assessed using ultrafast ultrasound and a principal strain estimator: In vitro evaluation and in vivo feasibility

Diya Wang[1,2] | **Boris Chayer**[2] | **François Destrempes**[2] | **Marc Gesnik**[2] | **François Tournoux**[2,3] | **Guy Cloutier**[2,4]

[1] School of Life Science and Technology, Xi'an Jiaotong University, Xi'an, China

[2] Laboratory of Biorheology and Medical Ultrasonics, Research Center, University of Montreal Hospital, Montreal, QC, Canada

[3] Department of Cardiology, Echocardiography Laboratory, University of Montreal Hospital, Montreal, QC, Canada

[4] Department of Radiology, Radio-Oncology and Nuclear Medicine, and Institute of Biomedical Engineering, University of Montreal, Montreal, QC, Canada

Correspondence
François Tournoux, Laboratory of Biorheology and Medical Ultrasonics, Research Center, University of Montreal Hospital, Montreal, QC H2X0A9, Canada.
Email: francois.tournoux@umontreal.ca
Guy Cloutier, Laboratory of Biorheology and Medical Ultrasonics, Research Center, University of Montreal Hospital, Montreal, QC H2X0A9, Canada.
Email: guy.cloutier@umontreal.ca

Funding information
Collaborative Health Research Program of the Natural Sciences and Engineering Research Council of Canada, Grant/Award Number: CHRP-462240-2014; Canadian Institutes of Health Research, Grant/Award Number: CPG-134748; Fonds Québécois de Recherche sur la Nature et les Technologies, Grant/Award Number: FQRNT-PR-189822

Abstract

Background: Noninvasive vascular strain imaging under conventional line-by-line scanning has a low frame rate and lateral resolution and depends on the coordinate system. It is thus affected by high deformations due to image decorrelation between frames.

Purpose: To develop an ultrafast time-ensemble regularized tissue-Doppler optical-flow principal strain estimator for aorta deformability assessment in a long-axis view.

Methods: This approach alleviated the impact of lateral resolution using image compounding and that of the coordinate system dependency using principal strain. Accuracy and feasibility were evaluated in two aorta-mimicking phantoms first, and then in four age-matched individuals with either a normal aorta or a pathological ascending thoracic aorta aneurysm (TAA).

Results: Instantaneous aortic maximum and minimum principal strain maps and regional accumulated strains during each cardiac cycle were estimated at systolic and diastolic phases to characterize the normal aorta and TAA. In vitro, principal strain results matched sonomicrometry measurements. In vivo, a significant decrease in maximum and minimum principal strains was observed in TAA cases, whose range was respectively 7.9 ± 6.4% and 8.2 ± 2.6% smaller than in normal aortas.

Conclusions: The proposed principal strain estimator showed an ability to potentially assess TAA deformability, which may provide an individualized and reliable evaluation method for TAA rupture risk assessment.

KEYWORDS
aorta deformability, principal strain, ultrafast imaging

1 | INTRODUCTION

Aortic aneurysm (AA) is a disease at a high risk of morbidity and mortality.[1] AAs are asymptomatic in most cases, but rupture occurs when the saccular wall cannot support the blood flow pressure anymore. In absence of rapid medical and surgical interventions, AA rupture leads to severe life-threatening internal hemorrhaging and death.[2,3] Even with prompt management, most of the patients with an AA rupture have a poor short-term prognosis.[1] Accordingly, thoracic and abdominal AA ruptures caused 9928 deaths in the United States in 2017[4] and about 167 200 deaths worldwide the same year.[5] According to current clinical guidelines, the maximum AA diameter and its annual growth rate are taken as risk criteria during follow-up.[3] However, these criteria have some limits since the AA rupture risk for some patients depends on multiple factors besides the size and growth rate of the AA. Thus, there is currently a major need for reliable methods that could provide a

more personalized rupture risk assessment.[6] Previous studies showed that aortic wall mechanical properties of AA change abnormally,[7] even at an early stage.[6] Aortic wall deformability and its evolution over time could be of additional value during patient's follow-up[8] and help clinicians to distinguish stable from prone to rupture aneurysms.[6]

Considering its noninvasiveness, portability, and real-time advantage, ultrasound strain imaging could have a key role in clinical practice for aortic deformability quantification and rupture risk assessment. Over the past two decades, several strain estimation core algorithms have been proposed for different applications, including space- and frequency-based cross-correlation,[9] tissue-Doppler imaging (TDI),[10] optical flow (OF),[11] and block matching.[12] Herein, axial strain can be well estimated by the normalized cross-correlation (NCC), which requires a high sampling rate in this direction and is limited by the computational load.[9] TDI is used to estimate large deformations in myocardial elastography but is limited by the Doppler Nyquist frequency and angle dependency.[13] Small displacements in vascular elastography can be calculated by instantaneous OF derivatives, which is, however, sensitive to decorrelation noise.[14]

Based on these core algorithms, various model-based strain estimators have been successively developed to improve the accuracy and robustness of axial strain, lateral strain, and shear strain assessments, including the Lagrangian speckle model estimator (LSME),[15] the least-squares strain estimator,[16] the no-prior reconstruction model estimator,[17] and other model-based affine strain algorithms.[18] Several advanced speckle tracking approaches have also been developed.[14,19–21] Considering advantages of TDI for large motion tracking and OF for small deformation conditions, TDI has been combined with the OF strategy to develop TDI-OF myocardial speckle tracking methods.[14,21]

Additionally in strain elastography, it is well known that coordinate-dependent strains (e.g., radial and circumferential strains) are estimated based on both the centroid position of the structure of interest and the coordinate system in a cross-sectional view.[22,23] These strain components are also unavailable in the long-axis direction.[18] Thus, a few teams have used principal strains to reduce the dependency of strain estimation on transducer's angle and structure's centroid.[18,23–25] However, because principal strains are constructed using all components of the strain tensor, robust estimators are required.

All ultrasound strain estimation and imaging techniques mentioned above are limited by echo decorrelation induced by out-of-plane motion artifacts between consecutive frames, and a common trade-off between spatial and temporal resolutions.[26] To overcome these limitations, ultrafast echocardiography has been developed to capture vascular and cardiac deformations at a very high frame rate.[27,28] Moreover, the coherent compounding diverging wave transmission strategy has been applied to ultrafast echocardiography for suppressing side lobes and improving spatial resolution.[19,28] Besides, our previous study applied a Doppler-based motion compensation (MoCo) strategy into the ultrafast echocardiography scheme to remove side-lobe artifacts between consecutive transmissions of diverging waves and to provide TDI simultaneously without extra computation.[29] Thus, the trade-off between spatial and temporal resolutions can be alleviated in ultrafast imaging.

Most of the AA strain studies focused on deformation evaluation of the abdominal aorta.[6,30–32] Only a few studies have assessed mechanical properties of the thoracic AA (TAA), especially at the level of the arch-type ascending aorta.[7] Strain estimates of ascending TAA are jeopardized by the difficulty to track rapid and large movements of the arch-type vascular structure, complex and large tissue deformations, and by the poor lateral resolution in the far-field region when using a phased array transducer. For these reasons, TAA strain imaging and rupture risk assessment are still a challenge in vascular elastography. Lubinski et al.[33] proposed a short-time correlation in elastography to improve robustness. Our group used this strategy to reduce variance to motion in the LSME algorithm in the case of carotid artery scanning.[27] This strategy may also be efficient for robust TAA strain elastography measurements.

Inspired by the prior art and under the hypothesis of strain linearity between consecutive frames in the context of ultrafast imaging, the major contribution of this paper was to propose an ultrafast time-ensemble regularized TDI-OF principal strain estimator to address specific and difficult challenges of thoracic ascending aorta strain estimation for assessing the deformability of aneurysms. To achieve the abovementioned important contribution, there were three key modifications and integrations with respect to the prior art. (1) The global cost function of spatial velocity terms in the TDI-OF myocardial tracking[14,21] was modified to be a regional residual quadratic TDI-OF cost function with spatiotemporal aortic displacement variables. (2) The modified TDI-OF cost function was further constrained by a time-ensemble regularized estimation strategy with a large temporal scale in the temporal domain and was then limited within a pair of thin arch-type aortic wall regions identified based on an OF estimation and Bayesian modeling in the spatial domain.[34] (3) A one-dimensional (1D) least-squares strain estimation[16] was improved and combined with the principal strain estimator[27] to form a 2D least-squares Gaussian-weighted principal strain estimator that was then integrated with the above improved TDI-OF tracking model to properly assess the curvilinear thoracic aorta deformability.

The outline of the paper is as follows. Section 2 presents the theoretical framework of the developed strain estimator, followed by Section 3 that includes the description of methods for in vitro and in vivo

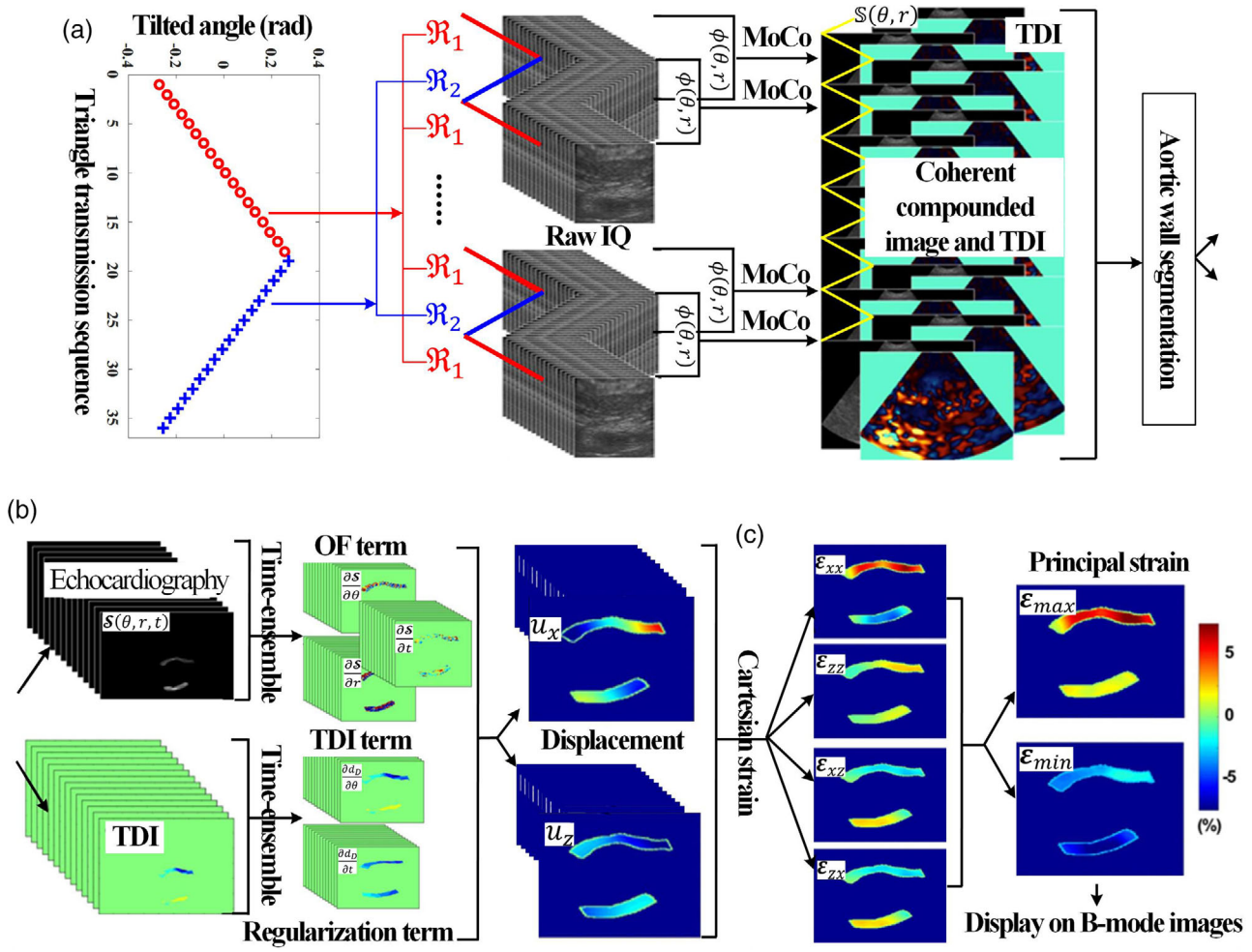

FIGURE 1 Schematic diagram of the 2D ultrafast time-ensemble regularized and combined tissue-Doppler imaging (TDI)–optical flow (OF) principal strain estimator. (a) Ultrafast aortic echocardiography, (b) time-ensemble regularized TDI–OF displacement estimator, and (c) 2D least-squares principal strain estimator

experiments (normal aorta and TAA conditions). Section 4 discusses about the procedures for data analysis. Results on the accuracy and feasibility of the developed strain estimator are described in Section 5. Finally, Sections 6 and 7 are dedicated to the discussions and conclusions.

2 | THEORETICAL FRAMEWORK

Figure 1 shows the schematic diagram of the developed strain estimator. Aortic images were reconstructed using ultrafast echocardiography as schematized in Figure 1(a). Then, the wall deformation of normal and TAA arteries was evaluated by using the proposed time-ensemble regularized TDI-OF displacement estimator, as illustrated in Figure 1(b), that was combined with a 2D least-squares principal strain estimator in Figure 1(c).

2.1 | Ultrafast aortic echocardiography

As developed in our previous study[29] and shown in Figure 1(a), the triangle transmission sequence for diverging waves combined with a Doppler-based MoCo strategy was used to remove artifacts induced by phase delays between transmissions. TAA scanning requires using a phased-array transducer with diverging waves. We briefly recall the theory; more details can be found in Porée et al.[29] The coherent compounded image $\mathbb{S}(\theta, r)$ considered the MoCo strategy in polar coordinates:

$$\mathbb{S}(\theta, r) = \sum_{m=1}^{M} \langle S_m \left\{ \theta, r + \left(m - \frac{M}{2} \right) \frac{\phi(\theta, r)}{4\pi} \frac{c}{f_0} \right\} e^{i\, m\phi(\theta, r)} \rangle \quad (1)$$

where

$$\phi\ (\theta, r) = \frac{1}{2} \angle\{\Re_1(\theta, r), \Re_2(\theta, r)\}. \quad (2)$$

In these equations, M denotes the number of tilted angles, $S_m(\theta, r)$ is the raw slow-time in-phase/quadrature (IQ) data at the mth tilted angle, $\phi(\theta, r)$ is the phase delay between transmissions, c is the speed of sound, and f_0 is the emitted pulse frequency of the ultrasound system. Diverging waves were coded as a triangle ascending subsequence $\Re_1$ and a descending subsequence $\Re_2$ with M tilted angles. The M tilted angles were transmitted at an equal space of 0.031 (rad) within an angular tilt of $\pm$0.28 (rad) and a width of $\pi/2$. Phases occurring in $\Re_1$ and $\Re_2$ subsequences yielded clockwise and counter-clockwise rotations of side lobe artifacts. The autocorrelation product in Equation (2) removed phase delay artifacts induced by rotations of side lobes in Equation (1) and provided TDI. After Doppler estimation, Equation (1) was computed to preserve a high Nyquist limit, as in Ref. 29.

2.2 | Aortic wall segmentation

For each loop of aortic B-mode images, the anterior and posterior walls were first manually delineated on a single frame (the middle one of the sequence), using an in-house graphical user interface. The contours of selected arch-type aortic walls were then propagated automatically using an algorithm based on motion estimation and Bayesian modeling, as described in Ref. 34. Since an initialization of labels directly based on quartiles of B-mode values was used rather than a random initialization, the expectation-maximization algorithm in Destrempes et al.[34] was simplified to a single run. Moreover, prior to the application of the least mean squares algorithm for motion estimation in Destrempes et al.,[34] a global translation of each aortic contour between two consecutive frames was estimated using an exhaustive search within a search range of $\pm$3 mm radially and $\pm$1 mm laterally. The segmentation algorithm was implemented in Visual C++.

2.3 | Time-ensemble regularized TDI-OF principal strain estimator

2.3.1 | Aortic displacement estimation

Angular $\mathbb{S}(\theta, r)$ data were oversampled with a 3:1 linear interpolation factor in the lateral direction (perpendicular to the compression wave direction) to improve the aorta lateral tracking. The 2D TDI-OF tracking model in Refs. 14 and 21 was constrained by the time-ensemble estimation strategy of Porée et al.[27] by using a large time scale $T = \{t_1, \ldots, t_n\}$ with $n = 14$ and a large overlap of 80% (see below the impact of changing the value of T). The aortic displacement vectors $\boldsymbol{u} = \{u_\theta, u_r\}$ within the temporal duration T were estimated by minimizing the regional residual and smoothness quadratic TDI-OF energy function within the segmented aortic wall regions, as in the following equations:

$$\begin{aligned}\hat{\boldsymbol{u}}\ (\theta, r) &= \arg\ \min\{J(\boldsymbol{u})\} \\ &= \arg\ \min[pJ_{\mathrm{D}}(\boldsymbol{u}) + (1-p)J_{\mathrm{O}}(\boldsymbol{u}) + \delta J_{\mathrm{R}}(\boldsymbol{u})]\end{aligned} \quad (3)$$

where the scalar $0 \le p < 1$ is an adjustment parameter set to 0.5 to balance the relative contribution of TDI and OF terms; $J_{\mathrm{D}}(\boldsymbol{u})$ and $J_{\mathrm{O}}(\boldsymbol{u})$ are TDI and OF terms, obtained from the Doppler field and $\mathbb{S}(\theta, r)$, respectively; $\delta = (1/\xi_c)^4$ is a weight term (see below), and $J_{\mathrm{R}}(\boldsymbol{u})$ is the regularization term. For aortic displacement tracking, the global TDI-OF energy function of spatial myocardial velocity terms in Refs. 14 and 21 was modified by regional weighted residuals of spatiotemporal aortic displacement variables in $J_{\mathrm{D}}(\boldsymbol{u})$ and $J_{\mathrm{O}}(\boldsymbol{u})$, as in the following equations:

$$J_{\mathrm{D}}\ (\boldsymbol{u}) = \omega_{\mathrm{D}} \left(\frac{\partial d_{\mathrm{D}}}{\partial \theta} u_\theta + \frac{\partial d_{\mathrm{D}}}{\partial t} - \frac{c \cdot \mathrm{PRF} \cdot \phi}{4\pi f_0 \cdot \mathrm{FR}} \right)^2 \quad (4)$$

$$J_{\mathrm{O}}\ (\boldsymbol{u}) = \omega_{\mathrm{O}} \left(\frac{\partial \mathcal{S}}{\partial r} u_r + \frac{\partial \mathcal{S}}{\partial \theta} u_\theta + \frac{\partial \mathcal{S}}{\partial t} \right)^2 \quad (5)$$

where ω_{D} is the weight of $J_{\mathrm{D}}(\boldsymbol{u})$, $d_{\mathrm{D}}\ (\theta, t) = \frac{c \cdot PRF \cdot \phi}{4\pi f_0 \cdot FR} / \| \frac{c \cdot \mathrm{PRF} \cdot \phi}{4\pi f_0 \cdot \mathrm{FR}} \|$ is the unitary displacement vector in the Doppler and temporal directions within the T scale, PRF is the pulse repetition frequency, FR is the frame rate after coherent compounding, ω_{O} is the weight of $J_{\mathrm{O}}(\boldsymbol{u})$, and $\mathcal{S}(\theta, r, t)$ is the 3D matrix within the T scale of $\mathbb{S}(\theta, r)$ data.

To avoid the formulation of an ill-posed problem, as done in Ref. 21, the summation of the squared modulus of the divergence and curl gradients of $\boldsymbol{u}$ in $J_{\mathrm{R}}(\boldsymbol{u})$ (Equation 3) was rewritten in the frequency domain according to Plancherel and Leffler's theories,[35] as in the following equation:

$$\delta J_{\mathrm{R}}\ (\boldsymbol{u}) = \delta \|\boldsymbol{\xi}\|^4 \|\tilde{\boldsymbol{u}}\|^2 = \|\boldsymbol{\xi}/\xi_{\mathrm{c}}\|^4 \|\tilde{\boldsymbol{u}}\|^2 \quad (6)$$

where $\boldsymbol{\xi}$ is the vector of spatial frequencies, $\tilde{\boldsymbol{u}}$ is the spatial Fourier transform of $\boldsymbol{u}$, and ξ_{c} is known as a spatial cut-off frequency to balance the TDI-OF terms, which was set to 24 times the wavelength after strain accuracy test based on ground truth sonomicrometry comparisons.

The weights ω_{D} in Equation (4) and ω_{O} in Equation (5) were updated iteratively, producing at each iteration an

updated solution of $\boldsymbol{u}_i$. The initial values of both $\omega_{D,1}$ and $\omega_{O,1}$ were set to $4V_N/|\sigma_D + 2V_N - FR|$. Here, V_N is the Nyquist Doppler velocity and $0 \le \sigma_D \le 2V_N$ is the Doppler standard deviation (STD). As in Ref. 21, parameters $\omega_{D,i}$ and $\omega_{O,i}$ were then iteratively updated using a bi-square function of the residual terms of Equations (4) and (5), which assigned small weights to data points with large residuals, to automatically adjust the weights of the TDI-OF model at each $\boldsymbol{u}_i$. Equation (3) was then solved as a least-squares problem to minimize the regional quadratic cost function. After updating the weights and solving Equation (3) iteratively, $\boldsymbol{u}_i$ was calculated as the average of displacement vectors within the T scale, and averaged values were then assigned to the center frame within T. The residuals of least-squares solution $\hat{\boldsymbol{u}}$ reached convergence after three iterations in this study.[21]

2.3.2 | 2D least-squares principal strain estimation

After coordinate transformation, the Cartesian 2D aortic displacement fields $\hat{\boldsymbol{u}} = \{u_x\ u_z\}$ in the lateral and axial directions were obtained, as shown in Figure 1. Inspired by 1D least-squares strain estimators[16] and the small instantaneous aortic strains (<1%) between frames within the T scale due to the use of high frame rate acquisition in this project, the displacement field $\boldsymbol{u}$ can be expressed as:

$$\begin{bmatrix} u_x \\ u_z \end{bmatrix} = \begin{bmatrix} \eta_x & \frac{\partial u_x}{\partial_x} & \frac{\partial u_z}{\partial_x} \\ \eta_z & \frac{\partial u_x}{\partial_z} & \frac{\partial u_z}{\partial_z} \end{bmatrix} \cdot \begin{bmatrix} 1 \\ x \\ z \end{bmatrix} = \begin{bmatrix} \eta_x & \varepsilon_{xx} & \varepsilon_{xz} \\ \eta_z & \varepsilon_{zx} & \varepsilon_{zz} \end{bmatrix} \cdot \begin{bmatrix} 1 \\ x \\ z \end{bmatrix} \tag{7}$$

where parameters $\{\eta_x\ \eta_z\}$ are constants to be estimated in lateral and axial directions, ε_{xx} and ε_{zz} are lateral and axial strains, respectively, and ε_{xz} and ε_{zx} are shear strains. Strains and constants in Equation (7) were estimated using a robust 2D least-squares estimator weighted by a convolution Gaussian window:

$$\begin{bmatrix} \hat{\eta}_x & \hat{\eta}_z \\ \hat{\varepsilon}_{xx} & \hat{\varepsilon}_{zx} \\ \hat{\varepsilon}_{xz} & \hat{\varepsilon}_{zz} \end{bmatrix} = \left[W^T G W\right]^{-1} W^T\ G \cdot \begin{bmatrix} u_{x_{i-w}} & u_{z_{i-w}} \\ \vdots & \vdots \\ u_{x_{i+w-1}} & u_{z_{i+w-1}} \end{bmatrix} \tag{8}$$

with

$$W = \begin{bmatrix} 1 & x_{i-w} & z_{i-w} \\ \vdots & \vdots & \vdots \\ 1 & x_{i+w-1} & z_{i+w-1} \end{bmatrix}. \tag{9}$$

In these equations, $\hat{(\cdot)}$ is an estimated solution, W is a $2w \times 3$ location matrix; w is the half window size of each strain estimate, which is determined by ξ_c; and G is a $2w \times 2w$ diagonal matrix, which contains Gaussian weights. The instantaneous Cartesian lateral, axial and shear strain estimates $\hat{\varepsilon}_{ij}$, at each point (x, z) within the weighted measurement window $(x_{i-w} : x_{i+w-1}, z_{i-w} : z_{i+w-1})$, were returned by the 2D least-squares strain estimator. Instantaneous aortic maximum and minimum principal strain maps $\boldsymbol{\varepsilon} = \{\varepsilon_{max}, \varepsilon_{min}\}$ were finally calculated with the following equations[36]:

$$\varepsilon_{max,min} = \frac{\hat{\varepsilon}_{xx} + \hat{\varepsilon}_{zz}}{2} \pm \sqrt{\left(\frac{\hat{\varepsilon}_{xx} - \hat{\varepsilon}_{zz}}{2}\right)^2 + \left(\frac{\hat{\varepsilon}_{xz} + \hat{\varepsilon}_{zx}}{2}\right)^2} \tag{10}$$

The $\boldsymbol{\varepsilon}$ strain maps were color coded and displayed in transparency on normalized B-mode images. To highlight strain maps only for display, a weight of 0.5 was used to normalize B-mode images on composite images. Besides, the directions $\theta_{\varepsilon_{max}}$ and $\theta_{\varepsilon_{min}}$ of principal maximum and minimum strains, where no shear strain acts on planes of principal strains,[23–25] were deduced from the following equations[27]:

$$\theta_{\varepsilon_{max}} = \frac{1}{2} \tan^{-1}\left(\frac{2\hat{\varepsilon}_{xz}}{\hat{\varepsilon}_{xx} - \hat{\varepsilon}_{zz}}\right) \tag{11}$$

$$\theta_{\varepsilon_{min}} = \theta_{\varepsilon_{max}} + \frac{\pi}{2} \tag{12}$$

Averages of principal strain directions within segmented regions of anterior and posterior walls were calculated and displayed by yellow arrows.

3 | EXPERIMENTS

3.1 | In vitro experiments

As shown in the in vitro experimental block diagram of Figure 2, two aorta-mimicking phantoms were fabricated (wall thickness = 3 mm and length = 145 mm). As shown in physical photos of Figure 2, inside diameters of the normal aorta were 22 mm, whereas those of the TAA phantom ranged from 24 to 52 mm. Each vessel was fabricated with homogeneous gel prepared using 7% per unit volume of polyvinyl alcohol (PVA) dissolved in pure water for the normal aorta, and 10% per unit volume in the case of the TAA, since the PVA concentration is a cofactor affecting stiffness.[37] Gels were mixed with graphite particles at 1% mass solutions to simulate acoustic backscatter properties of aortic tissues. Each gel solution was poured in a mold fabricated with a 3D printer (Dimension Elite, Stratasys

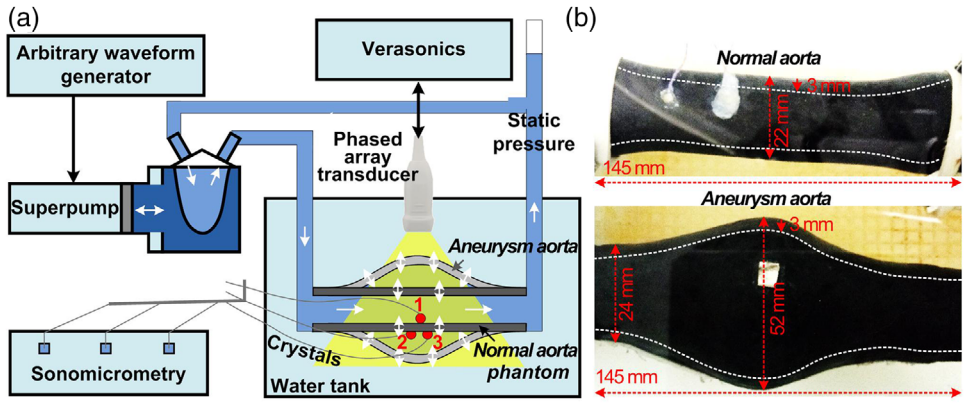

FIGURE 2 (a) In vitro experimental block diagram of aortic strain evaluation in (b) two dynamic normal and ascending thoracic aorta aneurysm (TAA) mimicking phantoms

Ltd, Eden Prairie, MN, USA). Polymerization with six freezing–thawing cycles allowed producing the compliant normal aorta mimicking phantoms in a temperature-controlled chamber designed in house, and polymerization with eight freezing–thawing cycles produced the TAA mimicking phantom.[38] Temperatures were ±20°C for freezing and thawing, respectively, of which respective duration was 510 min in each cycle. The outer mold had two halves and the inner mold was easily broken into four empty parts to get the phantom out without damage.

The normal and TAA phantoms were connected at each end to a hydraulic pulse duplicator within a left ventricular model (Superpump system, model #10647; Vivitro Inc., Victoria, BC, Canada), and stroke volumes were adjusted to 50, 70, and 83 ml, respectively. The in vitro cardiac rate was set to 60 beats per min (bpm), which was controlled with a sine wave produced by a waveform generator (model #33250A; Agilent Inc., Santa Clara, CA, USA). In vitro strain data on repeated experiments (normal aorta: $n = 6$, TAA: $n = 6$) were obtained by processing echoes recorded with a research scanner (V-1-128; Verasonics Inc., Redmond, WA, USA) equipped with a 64-element phased-array transducer (P4-2; ATL Ultrasound Inc., Bothell, WA, USA). Moreover, three piezoelectric crystals of 2 mm in diameter (marked 1, 2, and 3 in Figure 2(a); Sonometric Corporation, London, Ontario, Canada) were pasted to the internal and external surfaces of the posterior wall of the normal aorta phantom. The sonomicrometry method recorded ground truth displacements between each crystal at a sampling frequency of 200 Hz to calibrate the phantom and evaluate the accuracy of the proposed principal strain estimator. Those measurements were done on the bottom wall and before ultrasound acquisitions to avoid shadowing artifacts on strain images and band aliasing interferences between the two systems, respectively.[39]

3.2 | In vivo experiments

Two healthy male volunteers and two patients were recruited. As shown in Table 1, three to four repeated data sets were acquired for each case to assess feasibility. All participants signed an informed consent, and the protocol was approved by the institutional review board on ethics of the University of Montreal Hospital Research Center. Subjects were instructed to hold breath during the 2-s ultrasound acquisitions to minimize motion artifacts induced by breathing on ultrasound images. Scanning was performed using the same Verasonics system and probe, as used in vitro. A parasternal long-axis view was used to scan the ascending aorta. During acquisitions, the heart rate and blood pressure were measured with a monitor (SureSigns VM4; Philips, Andover, MA, USA). The blood pressure was not acquired for young participants.

3.3 | Experimental ultrasound acquisitions

A series of circular diverging waves with a short burst of two wavelengths at a maximum voltage of 30 V and $M = 36$ tilted angles were generated by the full array aperture of the P4-2 transducer, at a f_0 of 2.5 MHz and a PRF of 4 kHz. Aortic raw IQ data in the long-axis direction were recorded at a sampling frequency of 5 MHz. Each acquisition of 2-s duration included at least two cardiac cycles. No apodization was used in transmission and reception. A standard delay-and-sum approach was used to beamform each single diverging wave echo $S_m(\theta, r)$ with an imaging depth of 14 cm. Aortic images were reconstructed at a compounding FR of 222.2 Hz with an overlap of 50% between each sequence of 36 angles (i.e., FR $= \frac{\text{PRF}}{M\times(1-\text{overlap})}$), for a field of view of $\pi/2$. Strain estimations are at this compounded FR.

TABLE 1 In vivo experimental information

Diagnosed aorta		Repeated acquisitions	Age (years)	Heart rate (bpm)	Blood pressure (mmHg)	
					Diastole	systole
Young	Normal	$n = 3$	31	51 ± 3	/	/
	TAA	$n = 3$	39	60 ± 2	/	/
Old	Normal	$n = 4$	57	71 ± 2	79 ± 1	117 ± 5
	TAA	$n = 3$	77	49 ± 2	59 ± 2	114 ± 9

3.4 | Acoustic energy output

To comply with in vivo imaging safety, the acoustic output was measured experimentally for the sequence used with the Verasonics system and probe. For the selected voltage and PRF, the scanner acoustic pressure at imaging depths ranging from 0.5 to 12 cm was measured with a 1-mm-diameter needle hydrophone (#SN976; Precision Acoustics, Dorchester, UK) in a water tank. The calibrated hydrophone signals were collected using an acquisition card (CompuScope #CS12501; Gage-Applied, Lachine, QC, Canada) at a sampling frequency of 100 MHz. Nonderated values (i.e., without considering attenuation) of the spatial peak time-averaged, pulse-averaged intensities and mechanical index were determined, as in Ouared et al.[40] All experiments were performed at room temperature.

4 | DATA ANALYSIS

All post-processing steps except the segmentation were performed using MATLAB 2016a (Mathworks Inc., Natick, MA, USA).

4.1 | Accuracy assessment with the normal aorta phantom

Considering that the calculation of the principal strain is mainly based on axial and lateral strains in Equation (10), their accuracy assessments were conducted. Measured displacements between each crystal of the sonomicrometry method were first used to calculate the ground-truth axial strain $\varepsilon_a(t) = \Delta D(t)/\overline{D(t)}$ within the in vitro posterior wall of the normal vessel. $D(t)$ is the time-varying instantaneous axial displacement curve, $\Delta D(t)$ indicates displacement differences between adjacent temporal samples of $D(t)$, and $\overline{D(t)}$ corresponds to the mean value of $D(t)$. Here, $D(t)$ was calculated based on the cosine law to ensure that the calculated displacement was in the axial direction, using the following equation:

$$D(t) = d_{12}(t) \cdot \sin\left\{\cos^{-1}\left[\frac{d_{12}^2(t) + d_{23}^2(t) - d_{13}^2(t)}{2d_{12}(t)\,d_{23}(t)}\right]\right\} \tag{13}$$

where $d_{12}(t), d_{13}(t)$, and $d_{23}(t)$ are instantaneous lengths between crystals #1 and #2, crystals #1 and #3, and crystals #2 and #3, respectively, as indicated in Figure 2(a). Moreover, the ground-truth lateral strain $\varepsilon_l(t) = \Delta d_{23}(t)/\overline{d_{23}(t)}$ was calculated. The parameter $\Delta d_{23}(t)$ indicates displacement differences between adjacent temporal samples, and $\overline{d_{23}(t)}$ corresponds to the mean value of $d_{23}(t)$. To evaluate the strain accuracy, correlation and Bland–Altman plot agreement analyses were conducted between sonomicrometry ground-truth $\varepsilon_a(t)$ and $\varepsilon_l(t)$ measures, and instantaneous axial and lateral strains estimated with the proposed method. A larger region that covered crystal locations was selected to suppress shadowing artifacts from crystal #1 when calculating estimated strains.

4.2 | Aortic deformability assessment using accumulated principal strains

Instantaneous maximum and minimum principal strain maps were averaged over a region within the anterior or posterior wall to obtain instantaneous maximum and minimum principal strains. Strains were then added up over time within a cardiac cycle from systole to the next systolic phase. It was reset to zero at each cycle. Since axial strains had the best periodicity among all computed strain components, this metric was selected to identify systolic and diastolic phases. Accumulated maximum and minimum principal strains were calculated within anterior and posterior walls and then synchronously displayed at the beginning of the systole phase. Strain ranges obtained by computing peak-to-peak values of accumulated principal strains of all cardiac cycles were used to evaluate the aorta deformability. Mean values and STD of these features were

compared between groups using paired *t*-tests. A p value < 0.05 was considered statistically significant. We assumed linearity of strains between images for the principal strain elastography algorithm because small instantaneous strains were computed at a high frame rate of 222.2 Hz to assess aorta deformability.

4.3 | Signal-to-noise ratios of strain maps

The elastographic signal-to-noise ratio (SNRe) of instantaneous strain maps was assessed as:

$$\mathrm{SNRe}_{\max,\min} = 10 \log \left[\overline{\varepsilon_{\max,\min}} / \mathrm{STD}\left(\varepsilon_{\max,\min}\right) \right] \quad (14)$$

where $\varepsilon_{\max,\min}$ is the instantaneous maximum and minimum principal strains within segmented regions of both anterior and posterior walls. SNRe without ($T = 1$) and with the time-ensemble estimation strategy for increasing duration of T from 1 to 22 were compared. The objective was to illustrate the impact of this strategy on the proposed strain estimator and to justify the selection of $T = 14$ in this project.

5 | RESULTS

5.1 | Comparison with sonomicrometry

Figure 3 displays examples of accuracy assessments of estimated aortic axial and lateral strains under a stroke volume of 50 ml. Cross-validation was conducted via correlation (panels c and e) and Bland–Altman (panels d and f) agreement analyses of estimated strains, with the proposed method, versus ground truth sonomicrometry strains. At stroke volumes of 50, 70, and 83 ml, the average correlation coefficient of axial strains was 0.98 ± 0.001, and the average STD in Bland–Altman agreement analyses remained under 0.22 ± 0.05%. The corresponding average correlation coefficient of lateral strains was 0.93 ± 0.02, and the average STD was 0.41 ± 0.13%. Although peaks of estimated strains were underestimated slightly due to the averaging effect within the larger region, the proposed method still had a high correlation and a good Bland–Altman agreement versus ground truth strains.

5.2 | Aortic instantaneous 2D principal strain maps

Figure 4 displays examples of in vitro instantaneous maximum and minimum principal strain maps of the normal aorta and TAA mimicking phantoms at systolic and diastolic phases in the long-axis view. Figure 5 shows in vivo instantaneous principal strain maps for a normal human aorta and a TAA of a pathological participant. As seen on these figures, the distance between anterior and posterior walls over time, herein called diameter curves, allowed identifying ejection time, systole, isovolumic relaxation time, and late diastole. In vitro and in vivo TAA time-varying diameters, averaged over time, were respectively 5.46 ± 0.39 cm and 4.03 ± 0.07 cm, and these values were 90 ± 22% and 48 ± 15% larger than diameters of normal aortas.

5.3 | Aortic accumulated principal strains

Examples of in vitro and in vivo accumulated maximum and minimum principal strains within anterior and posterior walls of normal aortas and TAAs, during one-to-two cardiac cycles, are presented in Figures 6 and 7. Durations of a cycle for in vitro and in vivo time-varying strains matched, respectively, the pump pulsation and cardiac rates of participants. Except for a few cases, absolute values of almost all positive and negative time-varying principal strain peaks (maximum and minimum components) under TAA conditions were smaller than corresponding strain components under normal conditions.

Figure 8 displays the range of maximum and minimum principal strains for normal aorta and TAA conditions in vitro, and in vivo for young and old groups. These values were averaged over the number of cycles and acquisitions available (given in Table 1). All accumulated maximum principal strain values had a range under TAA conditions that was smaller than the corresponding one for normal aortas in Figure 8(a). Compared with maximum principal strain ranges within anterior and posterior walls of normal aortas, corresponding ranges of in vitro TAA were 11.4 ± 2.5% ($p < 0.05$) and 17.4 ± 3.3% ($p < 0.05$) smaller, respectively; corresponding ranges of in vivo young TAA were 1.3 ± 1.2% and 11.2 ± 4.5% ($p < 0.05$) smaller, respectively; and corresponding ranges of in vivo old TAA were 3.9 ± 0.8% ($p < 0.05$) and 2.4 ± 0.4% ($p < 0.05$) smaller, respectively. Similar trends were seen for minimum principal strain ranges in Figure 8(b). Compared with minimum principal strain ranges within anterior and posterior walls of normal aortas, corresponding ranges of in vitro TAA were 8.8 ± 1.4% ($p < 0.05$) and 12.3 ± 2.2% ($p < 0.05$) smaller, respectively; corresponding ranges of in vivo young TAA were 4.3 ± 3.1% ($p < 0.05$) and 6.8 ± 1.9% ($p < 0.05$) smaller, respectively; and corresponding ranges of in vivo old TAA were 8.4 ± 1.6% ($p < 0.05$) and 8.5 ± 2.4% ($p < 0.05$) smaller, respectively. Note that in vitro and in vivo strain waveforms are different and their strain ranges are also slightly different due to differences in aorta shapes and driving pressure conditions between them.

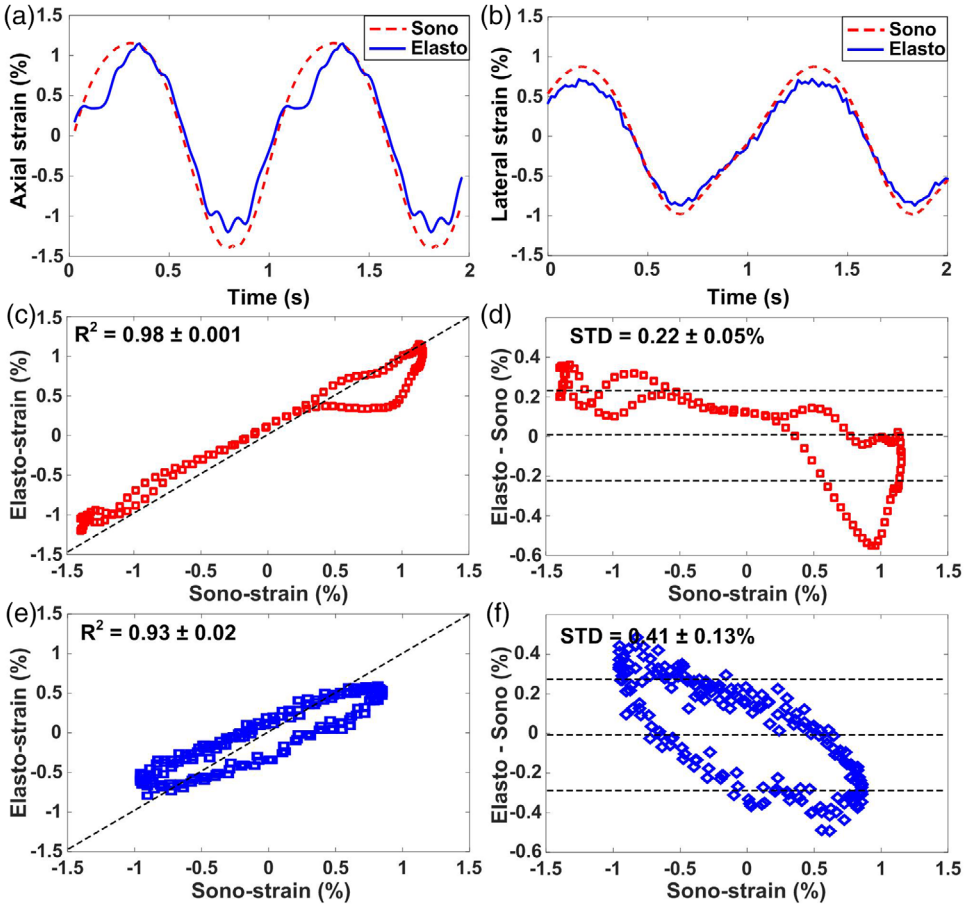

FIGURE 3 Accuracy assessment of the estimated aortic strain using sonomicrometry as the ground truth reference. In vitro instantaneous (a) axial and (b) lateral strains measured by sonomicrometry and estimated with the proposed method ($\hat{\varepsilon}_{zz}$ and $\hat{\varepsilon}_{xx}$ components) in the normal aorta phantom; (c) correlation and (d) Bland–Altman agreement analysis between axial strains; (e) correlation and (f) Bland–Altman agreement analysis between lateral strains. The measured strains using sonomicrometry and estimated strains using the proposed estimator are denoted "Sono" and "Elasto", respectively

5.4 | Acoustic energy output

With Verasonics scanner settings and probe described in Section 3.3, maximum values of the spatial peak time-averaged, pulse-averaged, and mechanical index of the transmitted acoustic intensity were 27.3 mW/cm^2, 6.1 W/cm^2, and 0.5. Those values are below the safety limits of the Food and Drug Administration standards.[41]

6 | DISCUSSION

6.1 | Relevance of using principal strains

The axial strain is often used for evaluating vascular wall deformations in the long-axis view.[9] However, as shown in the schematic diagram of Figure 9(a), aortas are not always experiencing compression and dilatation parallel to the wave propagation direction. Consequently, Eulerian and Lagrangian coordinate systems do not match, and the angulation θ varies with time and is amplified in the case of a TAA. To show the importance of mapping principal strains in this study, we present in Figures 9(b) and 9(c) time-varying values of accumulated axial strain and accumulated maximum and minimum principal strains, in the case of a normal aorta and a patient with a TAA. For the normal case, maximum and minimum principal strain ranges were 2.7 and 2.6 times larger than the axial strain range, whereas those values were 8.3 and 6.5 times more important than the range of axial strains in the case of the TAA.

The axial strain within the ascending aorta is underestimating the true mechanical deformation experienced by the vascular wall because of the angle dependency of this metric. Additionally, radial and circumferential strains are unavailable due to the uncertain centroid position of the arch-type structure in the polar coordinate system for a long-axis view.[24] Therefore, compared with axial, radial, or circumferential strain components, aortic principal strains not only overcame limitations of the centroid position of the structure of interest in

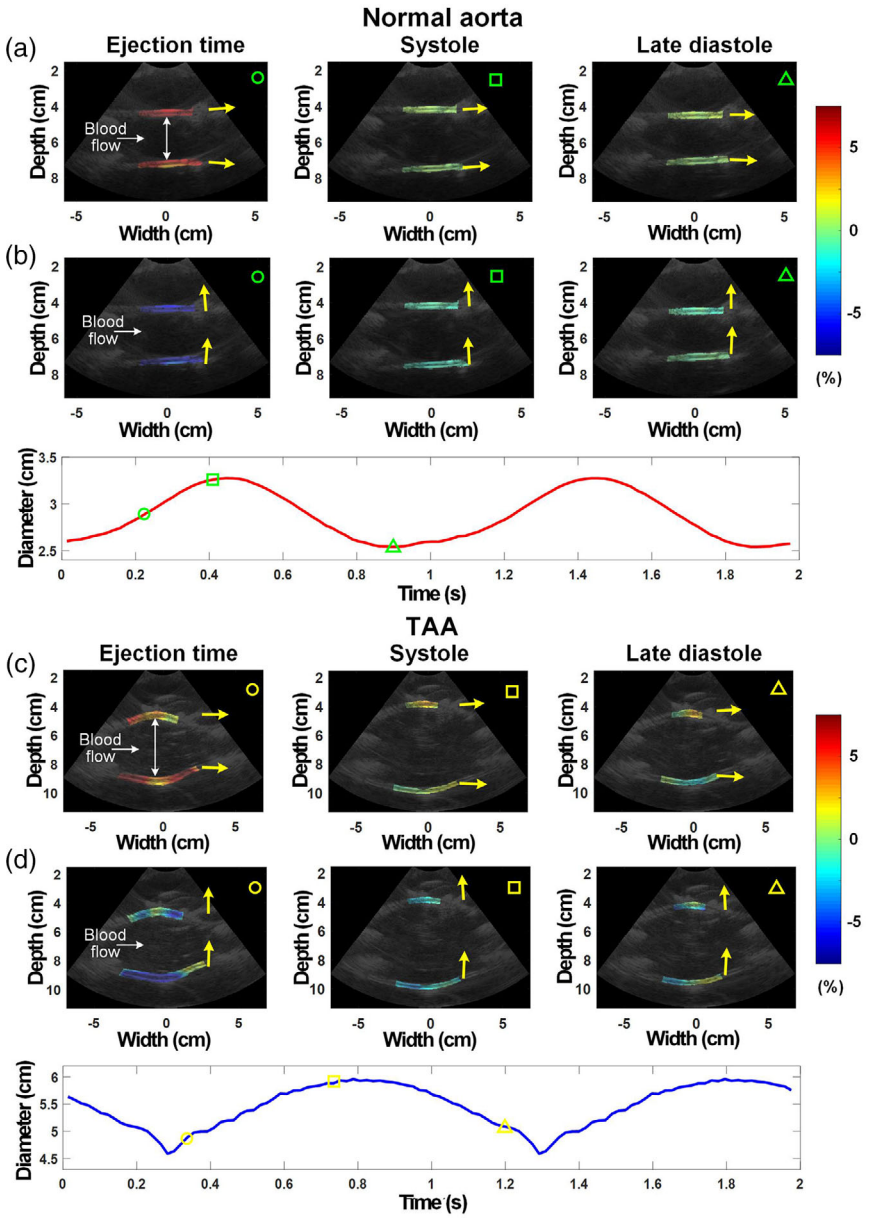

FIGURE 4 Examples of in vitro aortic deformability evaluations for the normal mimicking aorta and TAA phantoms using the proposed strain estimator. Instantaneous (a) maximum and (b) minimum principal strain maps of the normal aorta phantom at cardiac phases corresponding to the ejection time, systole, and late diastole. Corresponding instantaneous (c) maximum and (d) minimum principal strain maps of the TAA phantom for the same cardiac phases. These phases are marked on the time-varying aortic diameter curves at the bottom. The principal strain directions of anterior and posterior walls are marked with yellow arrows

polar coordinates,[23] but also provided the largest ranges among estimated strains, which agrees with previous studies.[18,23] Moreover, principal strains could visualize principal strain directions.[23–25] Principal strain directions and their STDs for all in vitro and in vivo cases were investigated initially. We observed that mean values of principal strain direction STDs of normal aortas were larger than those of TAA conditions. More detailed investigations of principal strain directions may require additional optimization and would deserve to be considered carefully in future works.

From another perspective, the proposed strain estimator could assess the aortic wall deformability from instantaneous principal strains computed between consecutive frames. All in vitro and in vivo computations resulted in instantaneous strains below 1%. When considering computations within the T scale (i.e., over T frames), instantaneous strain maps resulted in pixel values reaching 7.5%, and after averaging those pixels within the segmented wall, instantaneous strain curves varied from 0.01% to 3.8% (e.g., the maximum reached 1.2% in the case of in vitro results of Figure 3(a)). Thus, both estimation advantages of the OF in the case of small motions and of TDI in the case of larger displacements were verified with the proposed TDI-OF principal strain estimator, which could characterize aortic deformability distribution within various ranges.

6.2 | Improvements of TDI-OF estimation models

Tavakoli et al.[14] and afterward Porée et al.[21] built a TDI-OF energy function to estimate cardiac motion and to

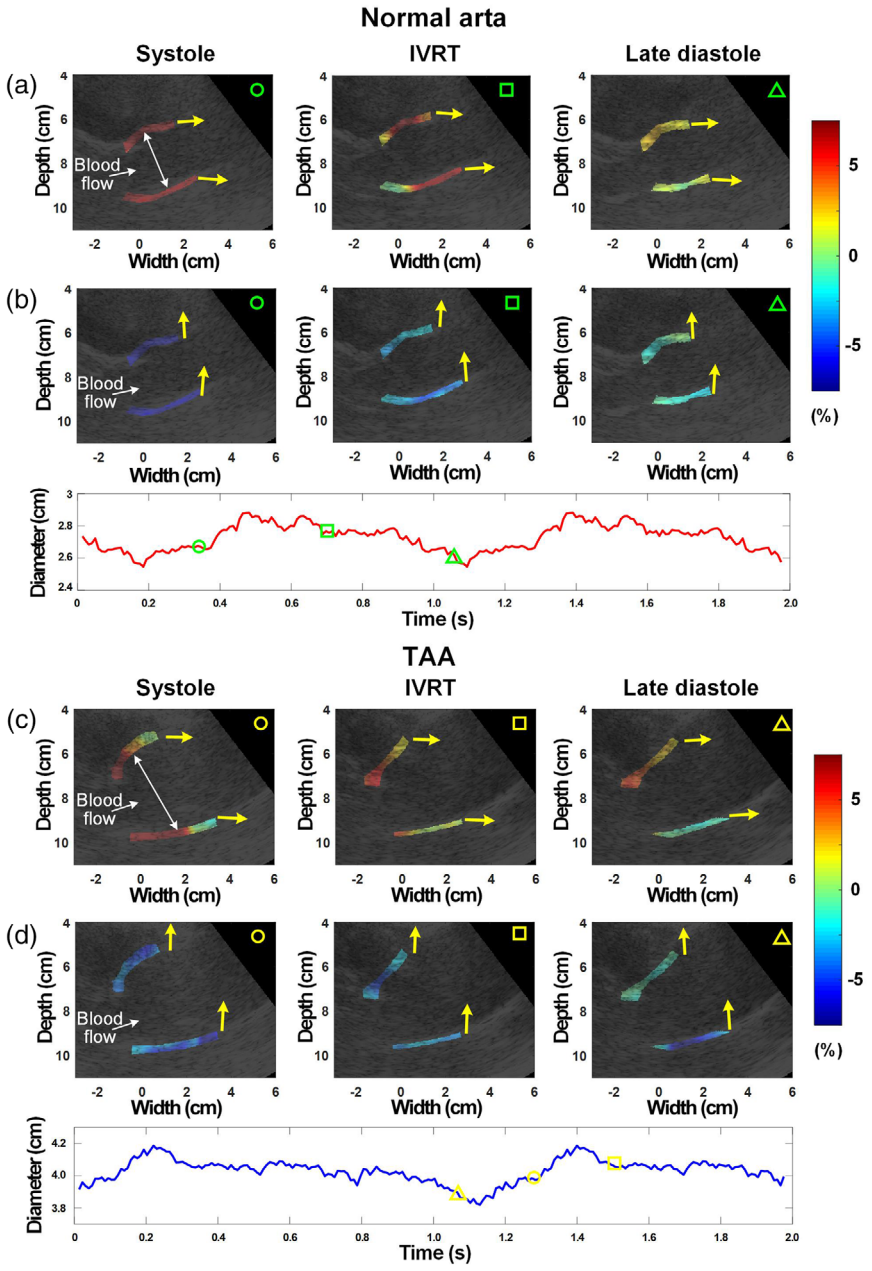

FIGURE 5 Examples of in vivo aortic deformability evaluations of the normal 31 years old volunteer and the TAA 39 years old patient using the proposed strain estimator. Instantaneous (a) maximum and (b) minimum principal strain maps of the normal aorta case at cardiac phases corresponding to systole, the isovolumic relaxation time (IVRT), and late diastole. Corresponding instantaneous (c) maximum and (d) minimum principal strain maps of the TAA case for the same cardiac phases. These phases are marked on the time-varying aortic diameter curves at the bottom. The principal strain directions of anterior and posterior walls are marked with yellow arrows

recover from it the myocardial velocity field at rest conditions. The framework for both of these models took advantage of the OF variation term, TDI velocity term, and smoothness energy term. But some algorithmic details differ between Tavakoli et al.[14] and Porée et al.[21] The OF variation term was normalized in Ref. 21, unlike in Ref. 14. The TDI velocity term was constrained by using a Geman–McClure penalizer in Ref. 14, while a constraint was imposed on the unitary velocity vector to be in the Doppler direction in Ref. 21. A common adjustment parameter p was used in Ref. 21 to balance the OF and TDI term but only the TDI term was limited by an individual adjustment parameter ß in Ref. 14. Moreover, a second-order regularizer based on the divergence and curl of the velocity field was used to smooth the whole flow field in Ref. 21, whereas outliers were rejected by the Geman–McClure penalizer in Ref. 14. Since local outliers appeared in aortic strain maps after removing the regularization term, this term was not only kept but also written in the current cost function.

In this study, we further considered the rapid and wide range of motion of the ascending aorta caused by the movement of the neighboring left ventricle and the complex and large tissue deformation of the compliant heterogeneous vessel wall. Therefore, a longer temporal scale than in Porée et al.[27] was used to constrain the TDI-OF model (we used $T = 14$ instead of eight successive frames). The global cost function of spatial velocity terms used for thicker myocardial tissue motions in Refs. 14 and 21 was modified by the regional residual

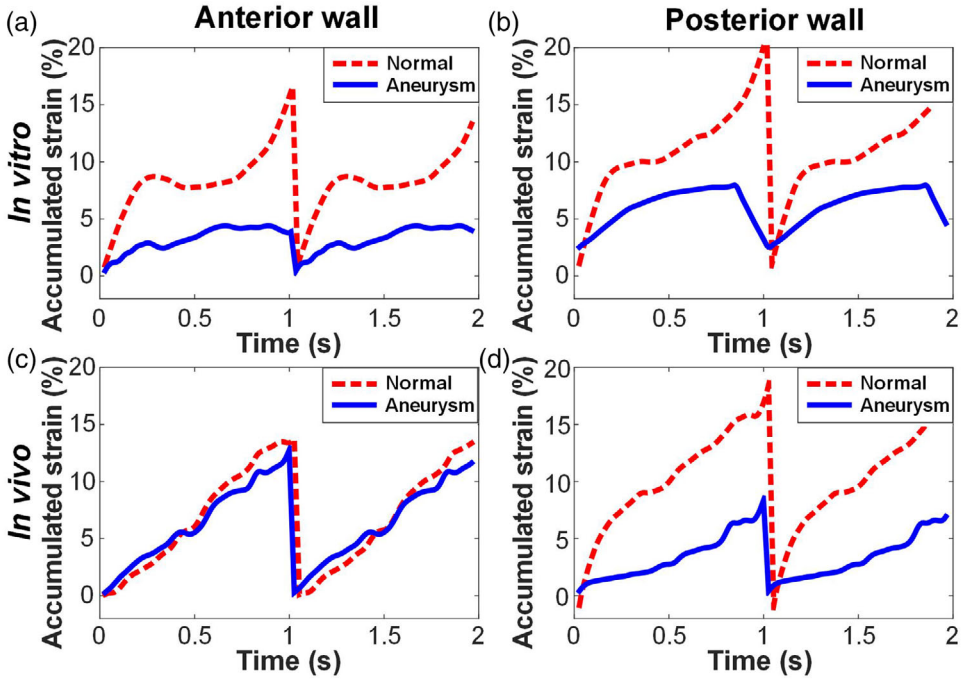

FIGURE 6 Four examples of (a and b) in vitro and (c and d) in vivo aortic strain evaluation using accumulated maximum principal strains during each cardiac cycle within anterior and posterior walls of a normal mimicking aorta phantom, and a TAA phantom, a normal aorta of a young volunteer, and a TAA of a patient

and smoothness quadratic cost function of spatiotemporal displacement vectors for the thinner arch-type aorta in this study. Its tracking was further constrained within a pair of small masks based on OF estimation and Bayesian modeling.[34] As shown in Figures 4 and 5, detailed spatially resolved deformations within the normal aorta and TAA walls were depicted on in vitro and in vivo maximum and minimum principal strain maps. These results further illustrated that the proposed ultrafast regularized TDI-OF principal strain estimator could capture rapid time-varying deformations under both normal aorta and TAA conditions.

Additional tests were done to prove the advantage of the time-ensemble strategy (Figure 10). The average SNRe of instantaneous maximum and minimum principal strain maps of all in vivo normal volunteers and TAA patients, and the corresponding average STDs, reached optimum values when using $T = 14$. Compared with results obtained without time-ensemble (i.e., $T = 1$ frame), the average SNRe of all in vivo instantaneous principal strain maps increased by 2.2 ± 0.3 dB when using $T = 14$. Average STDs of the corresponding SNRe decreased by 5.5 ± 1.4 dB with $T = 14$. As also noticed from Figure 10, further increasing the time-ensemble beyond 14 frames could degrade the SNRe and STD because considering too many consecutive frames for strain estimation negatively impacted robustness. According to the above SNRe evaluation, $T = 14$ was considered suitable in this study. Moreover, based on estimated correlation coefficients and STDs between measured ground truth and estimated axial strains, the parameter tuning was investigated by adjustment of p between 0 and 0.9, and δ between 1/0.5 mm^{-1} to 1/20 mm^{-1} in our preliminary studies. Thus, contributions of TDI, OF, and regularization terms were also compared. Note that the proposed energy function without the TDI term was studied when p was set to 0. However, when p was set to 1 to obtain the proposed energy function without the OF term, this resulted in an ill-posed problem since TDI displacements were only available along the Doppler direction.[21] After the above evaluations, p was set to 0.5 and ξ_c was set to 24 times the wavelength (where $\delta = (1/\xi_c)^4$), which provided the highest correlation coefficient, and accordingly the lowest STD. These improvements turned out to be more robust for the large displacement estimation of arch-type aorta for all cine loops, even at the condition of low but acceptable imaging quality.

6.3 | Potential impact of out-of-plane motions

Since the ascending aorta is adjacent to the left ventricle, the large torsional movement of the beating heart is impacting the motion of the aorta. This is likely favoring 3D rapid periodic out-of-plane motion of the ascending aorta, when compared with other vessels such as the

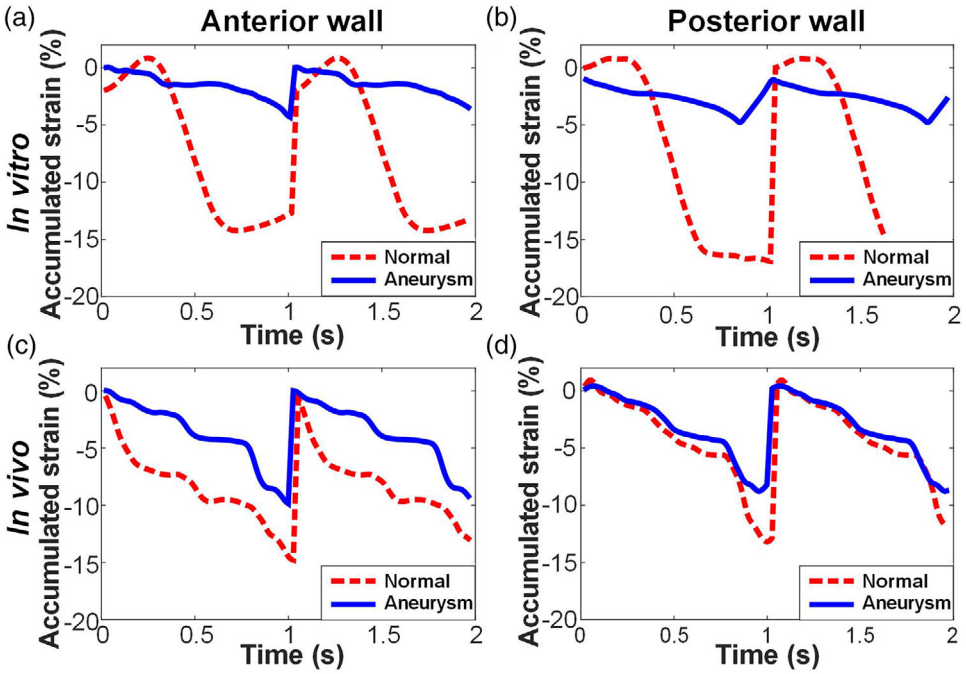

FIGURE 7 Four examples of (a and b) in vitro and (c and d) in vivo aortic deformability evaluation using accumulated minimum principal strains during each cardiac cycle within anterior and posterior walls of samples presented in Figure 6

abdominal aorta or carotid artery. The echo decorrelation induced by out-of-plane motion artifacts between consecutive frames could result in unstable and inaccurate strain estimation, which had been improved by the ultrafast imaging method (less movement between frames). Out-of-plane motion artifacts within the T scale were further reduced by the time-ensemble regularization strategy of the proposed strain estimator. As observed in this study (Figure 9(a)), the average thickness of aortic walls was about 3 mm and its translational movement was in a range above 1.2 cm during a cardiac cycle, especially for anterior walls. The average displacement between frames was about 10 μm; consequently, the TDI that is based on the autocorrelation has the same jitter and bias levels as the NCC, as described in Refs. 29 and 42. Moreover, TDI-OF has a lower variance and a higher agreement for motion estimation than NCC, TDI, and OF methods.[21] TDI was also obtained directly from Equation (2) without extra algorithm or computation, which was time efficient. Due to those reasons, the proposed energy function considered TDI rather than NCC.

As shown in Figure 10, strain maps without the time-ensemble estimation ($T = 1$) had the lowest SNRe and highest STD in all cases. Thus, the regularized TDI-OF and time-ensemble estimation strategies could be useful to reduce echo decorrelation produced by out-of-plane motions, while overcoming structure centroid and coordinate system dependency limitations. To minimize the influence of out-of-plane motion artifacts, 3D elastography and speckle tracking algorithms were developed using conventional 1D array transducers.[43,44] Recently, various 2D matrix arrays were designed and 3D tracking and strain estimation strategies were proposed to improve the accuracy and robustness of vascular (including the abdominal AA) and myocardial strain estimations.[6,45] But 3D elastography is still challenged by the large depth of TAA and the poor echogenicity in some patients.[6] The frame rate and spatial resolution are other limitations of 3D imaging using 2D arrays. With 3D system technical improvements, it would be relevant to expand, in future works, the proposed TDI-OF principal strain estimator for 3D imaging.

6.4 | Low lateral resolution in aortic echocardiography

The accuracy and robustness of strain estimation also depend on spatial resolution, especially lateral resolution.[28] The low center frequency and small aperture of phased arrays compared with linear arrays are impacting lateral resolution. This is further degraded at increasing imaging depth.[2] Therefore, improving lateral resolution in aortic echocardiography when using phased array transducers remains a challenge in 2D or 3D motion estimation, as well as in deformability and rupture risk evaluation. By using high-frame-rate imaging, multi-line transmits,[46] synthetic apertures,[47] coherent compounding plane waves,[18,26,27] and coherent

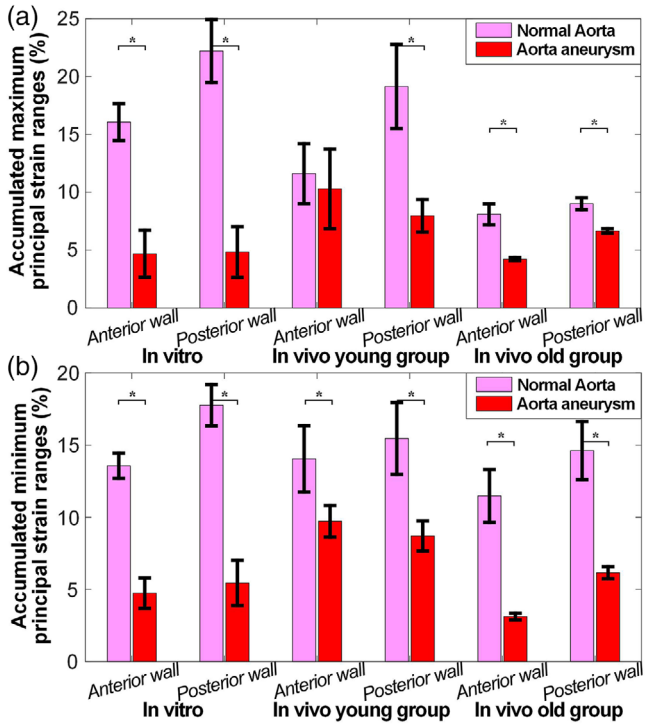

FIGURE 8 Statistical comparisons of accumulated (a) maximum principal strains and (b) minimum principal strains for normal aorta and TAA conditions in 12 in vitro samples, six samples from young volunteers, and seven samples from old participants

compounding diverging waves,[19,28] higher lateral resolution has been achieved for vascular and cardiac strain assessments. In this study, the contrast and spatial resolution of aortic echocardiography were improved by the coherent compounding diverging wave imaging technique. Sidelobe artifacts and phase delays induced by large tilted angle diverging wave transmissions were also reduced by the triangle transmission sequence combined with the Doppler-based MoCo strategy, which was proposed in our previous study.[29] Moreover, a cross-range interpolation was used in the proposed estimator to further improve strain estimation robustness.[27]

6.5 | Limitations of the linear strain assumption

As introduced earlier, instantaneous strains between frames were below 1%, thanks to the ultrafast imaging sequence used. By using the time ensemble strategy with $T = 14$, estimated instantaneous principal strains could reach 7.5% at given spatial locations within segmented vessel wall areas. Consequently, even if linear strain conditions could be assumed between frames, nonlinear effects could exist for estimates with $T = 14$. Future works should thus aim at replacing Equation (7) with its nonlinear counterpart to avoid biased estimates under large deformation conditions. Note, however, that cardiac strain imaging using speckle tracking, which is now a method implemented on clinical ultrasound scanners, does consider linear strain conditions, even with standard beamforming at frame rates typically below 100 Hz.[20,39]

6.6 | Clinical implication of this work

Elastin fiber fragmentation and smooth muscle cell disarray in innate or pathological conditions result in abnormal changes in aortic deformability.[48] The decrease of the aortic deformability and the corresponding increase of stiffness with aging have been observed in AA patients using noninvasive vascular elastography.[49] The abdominal AA pathology causes an early and significant decrease in aortic deformability even after considering the arterial pressure and aging effects.[6] Thoracic aortic deformability is also altered by cardiovascular diseases and exacerbates in innate or pathological conditions.[7] In the current study, a significant decrease in deformability (quantified by using maximum and minimum principal strains and their strain ranges) was observed under TAA conditions using the proposed estimator. However, although the presence of intraluminal thrombus in TAA is a rare phenomenon compared with abdominal AA,[50] regional strain assessment instead of averaging strain values over the whole segmented wall might be favorable considering the known impact of thrombosis on vessel mechanical properties.[51,52]

The observed smaller principal strains in patients with a TAA in this study suggest that aorta strain could be monitored during follow-up and have an additional clinical value in assessing the TAA rupture risk. If such a hypothesis becomes clinically proven in the future, we can assume that a decrease in TAA deformability over some thresholds (which will need to be defined) during the follow-up of a patient could lead to a preventive intervention to avoid a potentially fatal rupture. Therefore, we believe this study suggests the clinical potential of our proposed 2D ultrafast regularized TDI-OF principal strain estimator, as an individualized tool to assess the TAA mechanical property.

7 | CONCLUSION

Making use of advantages provided by TDI and OF techniques, an ultrafast regularized TDI-OF principal strain estimator was proposed to characterize the ascending aorta in vitro and in vivo and to assess differences in strain values between two normal aortas and two TAA cases. The proposed principal strain estimator overcame the coordinate system dependency of affine strains that is particularly relevant in the context of the thoracic aorta geometry. Therefore, the proposed principal strain estimator may provide an individualized and

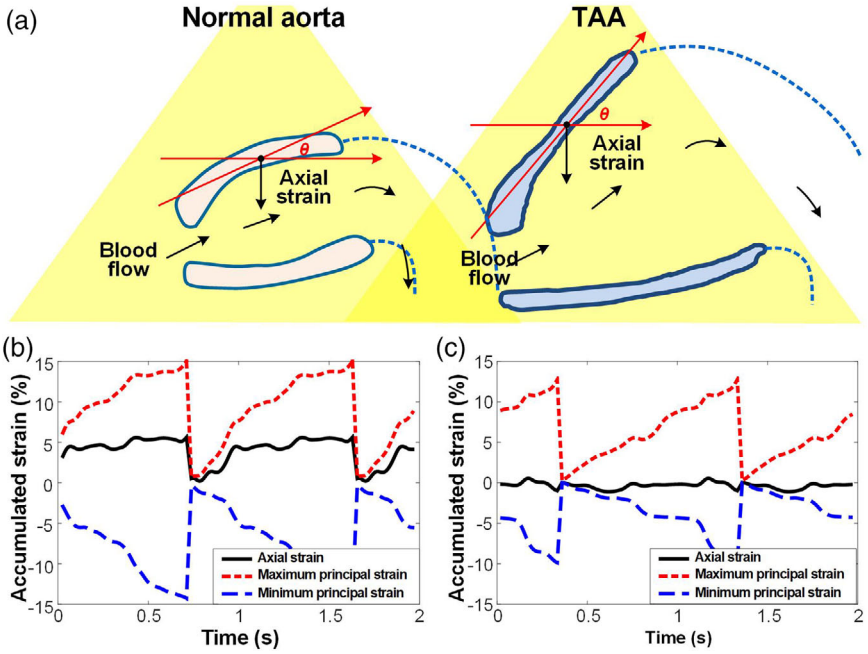

FIGURE 9 (a) Schematic diagram of the angulated deformation of the aortic wall with respect to the wave propagation direction. (b and c) Comparison between accumulated axial strain, and accumulated maximum and minimum principal strains, within anterior walls for (b) a normal aorta of a volunteer and (c) a TAA of a patient

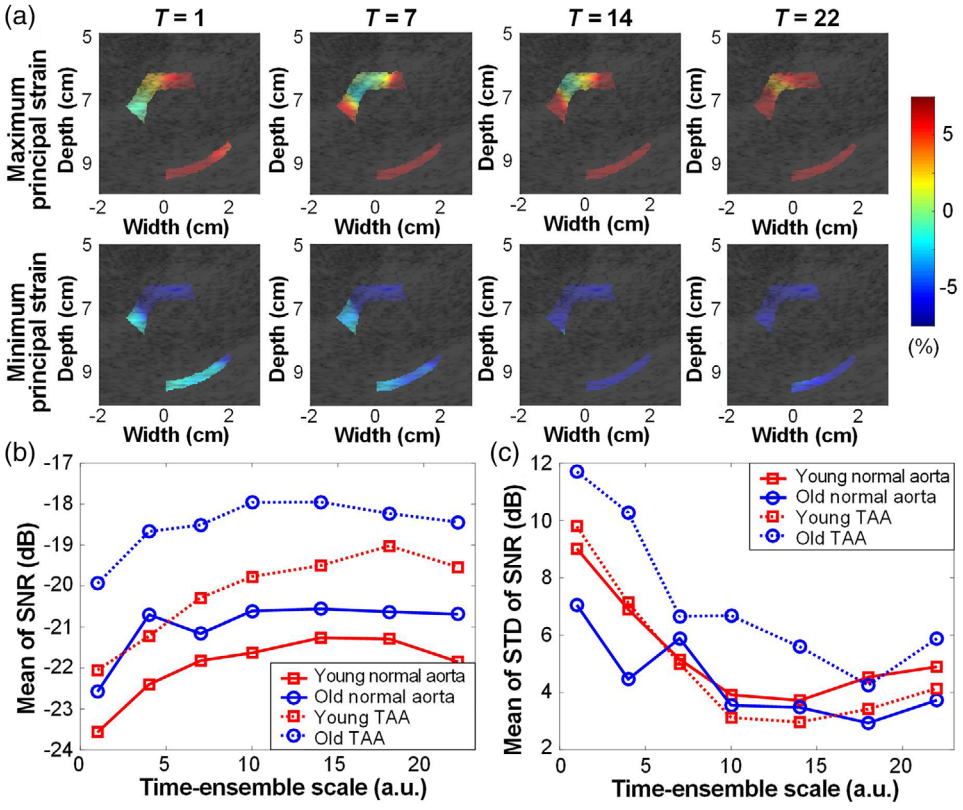

FIGURE 10 (a) Examples of instantaneous maximum and minimum principal strain estimation of the normal 57 years old volunteer without ($T = 1$) and with ($2 \leq T \leq 22$) the time-ensemble estimation strategy. (b) Mean and (c) standard deviation (STD) of elastographic signal-to-noise ratio (SNR) computed over all in vivo young and old normal and TAA cases

reliable evaluation method for aortic mechanical property characterization, which may be useful clinically for the early and timely assessment of TAA deformability and rupture risk during follow-up. However, additional investigations with more clinical cases would be necessary to determine the true impact of the proposed TDI-OF principal strain estimator. Indeed, the current study included phantom datasets but was limited to an in vivo proof-of-concept on a few cases.

ACKNOWLEDGEMENTS

This work was supported by the Collaborative Health Research Program of the Natural Sciences and Engineering Research Council of Canada (CHRP-462240-2014) and of the Canadian Institutes of Health Research (CPG-134748), and by a team grant of the Fonds Québécois de Recherche sur la Nature et les Technologies (FQRNT-PR-189822).

CONFLICT OF INTEREST

The authors have no conflicts to disclose.

DATA AVAILABILITY STATEMENT

Ultrasound data might be available upon request.

REFERENCES

1. Forsdahl SH, Singh K, Jacobsen BK. Risk factors for abdominal aortic aneurysms. *Circulation*. 2009;119(16):2202-2208.
2. Nandlall SD, Konofagou EE. Assessing the stability of aortic aneurysms with pulse wave imaging. *Radiology*. 2016;281(3):772-781.
3. Moll FL, Powell JT, Fraedrich G, et al. Management of abdominal aortic aneurysms clinical practice guidelines of the European society for vascular surgery. *Eur J Vasc Endovasc Surg*. 2011;41:S1-S58.
4. Centers for Disease Control and Prevention, National Center for Health Statistics. Underlying cause of death, 1999–2017 on CDC WONDER online database. 2019. Available on line: http://wonder.cdc.gov/ucd-icd10.html
5. Roth GA, Abate D, Abate KH, et al. Global, regional, and national age-sex-specific mortality for 282 causes of death in 195 countries and territories, 1980–2017: a systematic analysis for the Global Burden of Disease Study 2017. *Lancet*. 2018;392(10159):1736-1788.
6. van Disseldorp EM, Petterson NJ, van de Vosse FN, van Sambeek MR, Lopata RG. Quantification of aortic stiffness and wall stress in healthy volunteers and abdominal aortic aneurysm patients using time-resolved 3D ultrasound: a comparison study. *Eur Heart J Cardiovasc Imaging*. 2018;20(2):185-191.
7. Sulejmani F, Pokutta-Paskaleva A, Ziganshin B, et al. Biomechanical properties of the thoracic aorta in Marfan patients. *Annals of Cardiothoracic Surgery*. 2017;6(6):610-624.
8. Chirinos JA. Arterial stiffness: basic concepts and measurement techniques. *J Cardiovasc Transl Res*. 2012;5(3):243-255.
9. Luo J, Konofagou EE. A fast normalized cross-correlation calculation method for motion estimation. *IEEE Trans Ultrason Ferroelectr Freq Control*. 2010;57(6):1347-1357.
10. Hoffmann S, Mogelvang R, Olsen NT, et al. Tissue Doppler echocardiography reveals distinct patterns of impaired myocardial velocities in different degrees of coronary artery disease. *Eur J Echocardiogr*. 2010;11(6):544-549.
11. Zakaria T, Qin Z, Maurice RL. Optical-flow-based B-mode elastography: application in the hypertensive rat carotid. *IEEE Trans Med Imaging*. 2010;29(2):570-578.
12. Barjatya A. Block matching algorithms for motion estimation. *IEEE Trans Evol Comput*. 2004;8(3):225-239.
13. Golemati S, Gastounioti A, Nikita KS. Ultrasound-image-based cardiovascular tissue motion estimation. *IEEE Rev Biomed Eng*. 2016;9:208-218.
14. Tavakoli V, Bhatia N, Longaker RA, Stoddard MF, Amini AA. Tissue Doppler imaging optical flow (TDIOF): a combined B-mode and tissue Doppler approach for cardiac motion estimation in echocardiographic images. *IEEE Trans Biomed Eng*. 2014;61(8):2264-2277.
15. Maurice RL, Ohayon J, Fretigny Y, Bertrand M, Soulez G, Cloutier G. Noninvasive vascular elastography: theoretical framework. *IEEE Trans Med Imaging*. 2004;23(2):164-180.
16. Kallel F, Ophir J. A least-squares strain estimator for elastography. *Ultrason Imaging*. 1997;19(3):195-208.
17. Richards MS, Doyley MM. Investigating the impact of spatial priors on the performance of model-based IVUS elastography. *Phys Med Biol*. 2011;56(22):7223-7246.
18. Li H, Porée J, Roy Cardinal MH, Cloutier G. Two-dimensional affine model-based estimators for principal strain vascular ultrasound elastography with compound plane wave and transverse oscillation beamforming. *Ultrasonics*. 2019;91:77-91.
19. Joos P, Porée J, Liebgott H, et al. High-frame-rate speckle tracking echocardiography. *IEEE Trans Ultrason Ferroelectr Freq Control*. 2018;65(5):720-728.
20. D'hooge J, Barbosa D, Gao H, et al. Two-dimensional speckle tracking echocardiography: standardization efforts based on synthetic ultrasound data. *Eur Heart J Cardiovasc Imaging*. 2015;17(6):693-701.
21. Porée J, Baudet M, Tournoux F, Cloutier G, Garcia D. A dual tissue-doppler optical-flow method for speckle tracking echocardiography at high-frame-rate. *IEEE Trans Med Imaging*. 2018;37(9):2022-2032.
22. Nayak R, Schifitto G, Doyley MM. Visualizing angle-independent principal strains in the longitudinal view of the carotid artery: phantom and in vivo evaluation. *Ultrasound Med Biol*. 2018;44(7):1379-1391.
23. Nayak R, Huntzicker S, Ohayon J, et al. Principal strain vascular elastography: simulation and preliminary clinical evaluation. *Ultrasound Med Biol*. 2017;43(3):682-699.
24. Cupps BP, Pomerantz BJ, Krock MD, et al. Principal strain orientation in the normal human left ventricle. *Ann Cardiothorac Surg*. 2005;79(4):1338-1343.
25. Meshram NH, Mitchell CC, Wilbrand SM, Dempsey RJ, Varghese T. In vivo carotid strain imaging using principal strains in longitudinal view. *Biomedical Physics Engineering Express*. 2019;5(3):035030.
26. Hansen HHG, Saris AECM, Vaka NR, Nillesen MM, de Korte CL. Ultrafast vascular strain compounding using plane wave transmission. *J Biomech*. 2014;47(4):815-823.
27. Porée J, Garcia D, Chayer B, Ohayon J, Cloutier G. Noninvasive vascular elastography with plane strain incompressibility assumption using ultrafast coherent compound plane wave imaging. *IEEE Trans Med Imaging*. 2015;34(12):2618-2631.
28. Grondin J, Sayseng V, Konofagou EE. Cardiac strain imaging with coherent compounding of diverging waves. *IEEE Trans Ultrason Ferroelectr Freq Control*. 2017;64(8):1212-1222.
29. Porée J, Posada D, Hodzic A, Tournoux F, Cloutier G, Garcia D. High-frame-rate echocardiography using coherent compounding with doppler-based motion-compensation. *IEEE Trans Med Imaging*. 2016;35(7):1647-1657.
30. Fromageau J, Lerouge S, Maurice RL, Soulez G, Cloutier G. Noninvasive vascular ultrasound elastography applied to the characterization of experimental aneurysms and follow-up after endovascular repair. *Phys Med Biol*. 2008;53(22):6475-6490.

31. Salloum E, Bertrand-Grenier A, Lerouge S, et al. Endovascular repair of abdominal aortic aneurysm: follow-up with noninvasive vascular elastography in a canine model. *Radiology*. 2016;279(2):410-419.
32. Petterson NJ, van Disseldorp EM, van Sambeek MR, van de Vosse FN, Lopata RG. Including surrounding tissue improves ultrasound-based 3D mechanical characterization of abdominal aortic aneurysm. *J Biomech*. 2019;85(6):126-133.
33. Lubinski MA, Emelianov SY, Donnell MO. Speckle tracking methods for ultrasonic elasticity imaging using short-time correlation. *IEEE Trans Ultrason Ferroelectr Freq Control*. 1999;46(1):82-96.
34. Destrempes F, Meunier J, Giroux MF, Soulez G, Cloutier G. Segmentation in ultrasonic B-mode images of healthy carotid arteries using mixtures of Nakagami distributions and stochastic optimization. *IEEE Trans Med Imaging*. 2009;28(2):215-229.
35. Plancherel M, Leffler M. Contribution à l'étude de la représentation d'une fonction arbitraire par des intégrales définies. *Rendiconti del Circolo Matematico di Palermo (1884-1940)*. 1910;30(1):289-335.
36. Mase GT, Mase GE. *Continuum Mechanics for Engineers*. London, UK CRC Press 1992:100.
37. Gautam UC, Pydi YS, Selladurai S, et al. A poly-vinyl alcohol (PVA)-based phantom and training tool for use in simulated transrectal ultrasound (TRUS) guided prostate needle biopsy procedures. *Medical Engineering and Physics*. 2021;96:46-52.
38. Fromageau J, Gennisson JI, Schmitt C, Maurice RL, Mongrain R, Cloutier G. Estimation of polyvinyl alcohol cryogel mechanical properties with four ultrasound elastography methods and comparison with gold standard testings. *IEEE Trans Ultrason Ferroelectr Freq Control*. 2007;54(3):498-509.
39. Hodzic A, Chayer B, Wang D, et al. Accuracy of speckle tracking in the context of stress echocardiography in short axis view: an in vitro validation study. *PLoS One*. 2018;13(3):e0193805.
40. Ouared A, Montagnon E, Kazemirad S, Gaboury L, Robidoux A, Cloutier G. Frequency adaptation for enhanced radiation force amplitude in dynamic elastography. *IEEE Trans Ultrason Ferroelectr Freq Control*. 2015;62(8):1453-1466.
41. ter Haar G. *The Safe Use of Ultrasound in Medical Diagnosis*. 3rd ed.. British Institute of Radiology; 2012.
42. Pinton GF, Dahl JJ, Trahey GE, Rapid tracking of small displacements using ultrasound. Paper presented at: IEEE International Ultrasonics Symposium; 2005;4:2062-2065.
43. Deprez JF, Brusseau E, Schmitt C, Cloutier G, Basset O. 3D estimation of soft biological tissue deformation from radio-frequency ultrasound volume acquisitions. *Med Image Anal*. 2009;13(1):116-127.
44. De Craene M, Marchesseau S, Heyde B, et al. 3D strain assessment in ultrasound (Straus): a synthetic comparison of five tracking methodologies. *IEEE Trans Med Imaging*. 2013;32(9):1632-1646.
45. Papadacci C, Bunting EA, Wan E, Nauleau P, Konofagou EE. 3D Myocardial elastography in vivo. *IEEE Trans Med Imaging*. 2017;36(2):618-627.
46. Tong L, Ramalli A, Tortoli P, et al. Wide-angle tissue Doppler imaging at high frame rate using multi-line transmit beamforming: an experimental validation in vivo. *IEEE Trans Med Imaging*. 2016;35(2):521-528.
47. Nayak R, Schifitto G, Doyley MM. Noninvasive carotid artery elastography using multielement synthetic aperture imaging: phantom and in vivo evaluation. *Med Phys*. 2017;44(8):4068-4082.
48. Halushka MK, Angelini A, Bartoloni G, et al. Consensus statement on surgical pathology of the aorta from the Society for Cardiovascular Pathology and the Association For European Cardiovascular Pathology: iI. Noninflammatory degenerative diseases-nomenclature and diagnostic criteria. *Cardiovasc Pathol*. 2016;25(3):247-257.
49. Oishi Y, Mizuguchi Y, Miyoshi H, Iuchi A, Nagase N, Oki T. A novel approach to assess aortic stiffness related to changes in aging using a two-dimensional strain imaging. *Echocardiography*. 2008;25(9):941-945.
50. Ciurus T, Undas A, Lelonek M. Unexplained thrombosis of the aortic arch with distal embolization in a patient with altered fibrin clot properties. *Arch Med Sci*. 2012;8(4):733-735.
51. Thubrikar MJ, Robicsek F, Labrosse M, Chervenkoff V, Fowler BL. Effect of thrombus on abdomnial aortic aneurysm wall dilation and stress. *J Cardiovasc Surg*. 2003;44(1):66-67.
52. Siobhan AOL, Kavanagh EG, Grace PA, McGloughlin TM, Barry JD. The biaxial mechanical behaviour of abdominal aortic aneurysm intraluminal thrombus: classification of morphology and the determination of layer and region specific properties. *J Biomech*. 2014;47(6):1430-1437.

How to cite this article: Wang D, Chayer B, Destrempes F, Gesnik M, Tournoux F, Cloutier G. Deformability of ascending thoracic aorta aneurysms assessed using ultrafast ultrasound and a principal strain estimator: In vitro evaluation and in vivo feasibility. *Med Phys*. 2022;49:1759–1775.
https://doi.org/10.1002/mp.15464